



HAL
open science

FIB-SEM based 3D tomography of micro-electronic components: Application to automotive high-definition LED lighting systems

Safa Nocairi, Nicolas Compère, Antonin Bermond, Christine Roucoules, Sergio Sao Joao, Matthieu Lenci, Guillaume Kermouche, Helmut Klöcker

► To cite this version:

Safa Nocairi, Nicolas Compère, Antonin Bermond, Christine Roucoules, Sergio Sao Joao, et al.. FIB-SEM based 3D tomography of micro-electronic components: Application to automotive high-definition LED lighting systems. *Microelectronics Reliability*, 2022, 137, pp.114749. 10.1016/j.microrel.2022.114749 . hal-03782555

HAL Id: hal-03782555

<https://hal.science/hal-03782555>

Submitted on 22 Sep 2022

HAL is a multi-disciplinary open access archive for the deposit and dissemination of scientific research documents, whether they are published or not. The documents may come from teaching and research institutions in France or abroad, or from public or private research centers.

L'archive ouverte pluridisciplinaire **HAL**, est destinée au dépôt et à la diffusion de documents scientifiques de niveau recherche, publiés ou non, émanant des établissements d'enseignement et de recherche français ou étrangers, des laboratoires publics ou privés.

1
2 **FIB-SEM based 3D tomography of micro-electronic components:**
3 **Application to automotive high-definition LED lighting systems**
4 Safa NOCAIRI ^(*)(3), *Nicolas Compère* ⁽²⁾, Antonin Bermond ⁽³⁾, Christine Roucoules ⁽¹⁾,

5 Sergio Sao-Joao ⁽³⁾, Matthieu Lenci ⁽³⁾, Guillaume Kermouche ⁽³⁾, Helmut Klöcker ⁽³⁾

6 ⁽¹⁾: Valeo Lighting Systems, 93000, Bobigny, France

7 ⁽²⁾: Manutech-USD, Bâtiment des Hautes Technologies, 20, Rue Professeur Benoît Lauras, 42000
8 Saint-Étienne, France

9 ⁽³⁾ Mines Saint-Etienne, Univ Lyon, CNRS, UMR 5307 LGF, Centre SMS, F - 42023 Saint-Etienne
10 France

11
12 **Abstract**

13 The first lead-free solders revealed as a weak part of electronic components and LED assemblies. In new
14 high definition lighting modules, assembling more than thousand elements (pixels) with a single mm-sized
15 motherboard is achieved by reflow soldering. During reflow, the distance between pixels and motherboard
16 controls the solder heights (10µm). After assembly, all the pixels are in a single plane. To ensure constant
17 solder heights, this plane has to be parallel to the motherboard. A small disorientation during reflow may
18 lead to severe solder damage prior to any use of the opto-electronic component. Present work presents
19 a novel non-destructive method for characterizing any chosen solder in the assembled component without
20 unpacking the latter.

21 A femtosecond motorized laser source is used for digging a hole in the LED above the selected solder.
22 Then a **Focused Ion Beam** facility allows to mill around this specific solder. The same FIB facility allows
23 making several hundred slices of controlled thickness and orientation in the solder material. During this
24 slicing operation, high-resolution inspection is done by FEG-SEM imaging. 3D tomographic reconstruction
25 of the solder is obtained by classical commercial software AVIZO. Finally, 3D damage in solder material
26 is illustrated by example results.

27 **Keywords:** characterize assembled LED, reflow, damage, Focused Ion Beam, Femtosecond Laser,
28 Very high resolution Tomography

29
30
31
32
33
34
35
36
37
38
39
40 *Corresponding author

41 safa.nocari@valeo.com

42
43

44 1. Introduction

45

46 Over the past fifteen years, LED lamps have become very common in automotive lighting due
47 to long service life and reasonable power requirements [1]. The first product families assembled with lead
48 free solders revealed significant fatigue damage in the solder material. Consequently, solders were
49 considered the weakest components. However, solders are essential for electric current supply as well
50 as thermal and mechanical reliability.

51 The microstructure of lead free solders [2-5], as well as their interfacial reaction with common
52 substrates [6, 7] were analyzed thoroughly. Gao et al. characterized intermetallics evolution in Sn-3.5Ag
53 based solders [8]. Ventura et al. analyzed the solidification kinetics of Sn-Cu solder alloys [9]. Phase
54 diagram prediction is still an active field in solder research [10]. Lee and Bieler presented two reviews on
55 lead-free solders in 2015 and 2017 [11, 12]. Mechanical reliability was considered an important issue right
56 from the beginning of lead free solder characterization. Several specific tests inside the SEM were
57 developed [13, 14]. In the first generation of lead free Cu/Sn solders bismuth segregation led to interfacial
58 embrittlement [15]. Zheng et al. addressed the reliability of several lead free solders [16]. Already in 2003,
59 Suo [17] laid the theoretical bases for all of solder reliability analyses. Since then, numerous new
60 contributions are constantly made [18]. These analyzes were dedicated to in depth characterization of a
61 single or a small number of solders.

62 Smart headlamps with an integrated camera are available since 2006 [19, 20]. This led to the
63 development of a 'matrix beam' with many pixels [21]. Meanwhile, modules consisting of 50-100 LEDs
64 allow minimizing glare by turning off the light emitted in specific directions. Wireless communication
65 technologies [22-24] leading to enhanced safety need lead to the development of *pixelated LEDs with*
66 *several thousand pixels assembled by reflow to a single motherboard*. Typical solder heights are in the
67 μm -range. The in plane dimensions of the motherboards are in the mm or cm-range. The final height and
68 shape of the solders is thus controlled by the reflow process. A small disorientation *during reflow may*
69 *lead to severe solder damage prior to any use of the opto-electronic component*. To the best of our
70 knowledge, no non-destructive inspection method of a particular solder after reflow exist. In present paper,
71 we present a novel inspection technique allowing *characterizing any chosen solder without disassembling*
72 *the opto-electronic component*. To demonstrate the feasibility of the method, the new characterization is
73 applied to one specific component with particular solder dimensions. However, these experimental
74 methods are adapted for characterizing solders with typical dimensions reaching from several tens of μm
75 to some mm.

76 A femtosecond motorized laser source is used for digging a hole in the LED above the selected
77 solder. Laser machining has been applied for more than 20 years in microelectronics [25]. Then a Focused
78 Ion Beam facility allows to mill around this specific solder [26]. The same FIB facility allows making several
79 hundred slices of controlled thickness and orientation in the solder material. During this slicing operation,
80 high-resolution inspection is done by FEG-SEM imaging. 3D tomographic reconstruction of the solder is
81 obtained by classical commercial software AVIZO. Finally, 3D damage in solder material is illustrated by
82 example results.

83 The paper is organized as follows. Section 2 explains the component architecture and reflow
84 assembling. The following section explains the experimental steps in detail. The fourth section presents
85 the main results with an emphasis on information gained by the combination of high-resolution SEM
86 images and 3D tomographic analysis applied to a particular component [27].

87

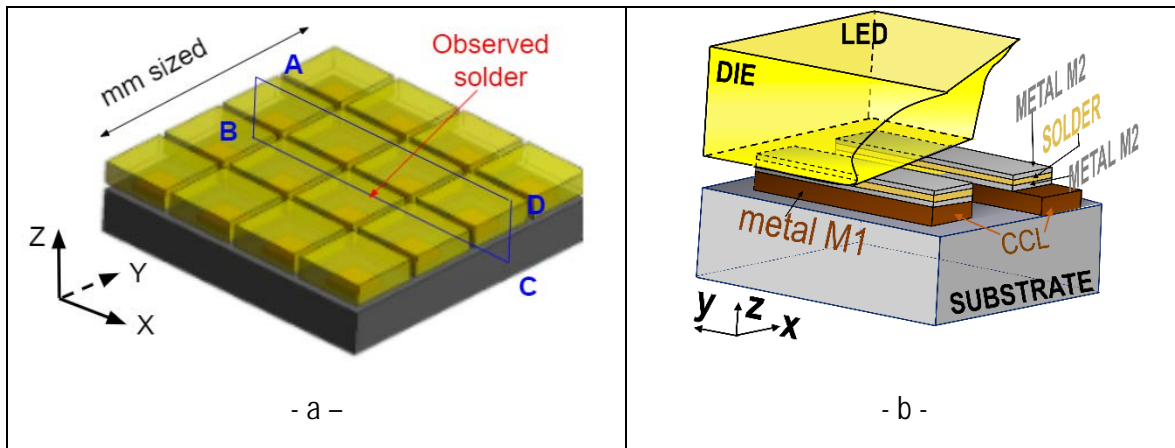
88 2. Component Architecture and Assembling

89

90 A new pixelated LED (Figure 1a) was designed to analyze the reflow with several hundred of
91 small micron-sized solders. The latter are connected to the substrate to allow electric current flow and
92 system cooling through interconnect joints. As illustrated in Figure 1b, each pixel contains two pads (PN
93 junctions). This architecture establishes a major step towards increased safety and vehicle-to-vehicle
94 communication.

95 After reflow (soldering), perfect functioning of each interconnect has to be guaranteed. However,
96 the close packed architecture increases the difficulty of the soldering process to a yet unknown level due
97 to the very small solder height and the huge die extensions. Effectively, small die rotations around the x-
98 or y-axis cause huge variations in solder height. The aim of this work is a 3D characterization of any
99 desired solder *in the assembled structure*. We have thus deliberately chosen this novel architecture to
100 highlight the efficiency of 3D tomographic characterization with SEM-typical resolutions. In the next
101 section, the principle of combined femtosecond laser local Die ablation followed by FIB milling of the
102 solder material will be given.

103



104 **Figure 1:** Schematic representation of high definition LED. (a) Overall architecture, (b) zoom in on a
105 single pixel.

106 3. Experimental

107 3.1. 2D SEM observations

108

109 Prior to 3D characterization of the solders, microscopic observations after reflow assembling
110 were made in a ZEISS SUPRA 55 VP Scanning Electron Microscope. First, the entire LED and then
111 specific cross sections were characterized. Cross sections were prepared by milling with a Jeol Cross
112 Polisher IB-19530CP using an Argon Ion beam. In a first step, the samples were cut with a diamond wire
113 saw to fit in the cross polisher chamber. In a second step, a mask, on top of the sample, reveals only the
114 part to be removed by the Argon beam. All details and parameters used for cross polishing are given in
115 table 2. After polishing with this new facility, samples were ready for SEM observations (table 1).

116 Figure 2a shows SEM observations before and after cross polishing with the optimized
117 parameters given in table 2. Observations were made in the plane ABCD (Figure 1a) perpendicular to the
118 y-axis. Figure 2b zooms on one pixel. The region of interest corresponds to the solder exhibiting a
119 heterogeneous distribution of micro-voids. These small micro-voids are difficult to characterize by X-ray
120 micro-tomography [27-29]. Fraczkiwicz et al. [30] applied high-resolution X-ray tomography with a pixel-
121 size of 100nm. However, the rotations needed for scanning limit these observations to single solders. A
122 full 3D high-resolution SEM based tomography of a solder *in the assembled LED* is developed in the next
123 paragraph.

124

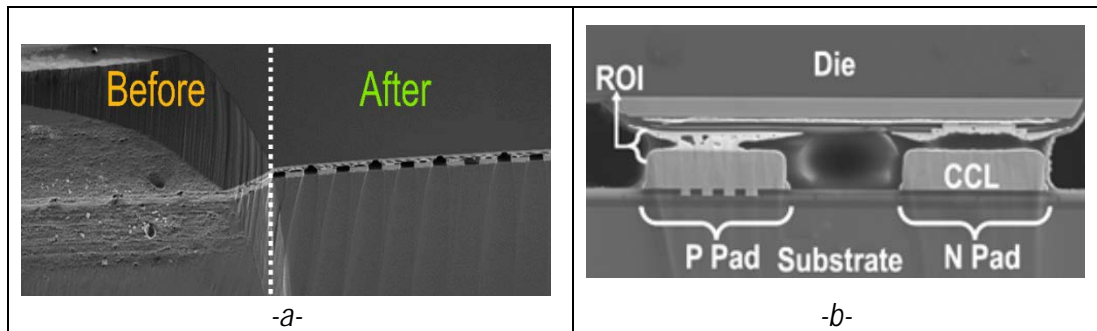


Figure 2: Sample after reflow. (a) SEM observation before and after cross polishing, (b) Zoom in on a single pixel depicting voids in the solder material (ROI).

3.2 Sample preparation for 3D Characterization

3.2.1. General outline of the method

After reflow, the LED architecture corresponds to the sketch in figure 3a. The upper part is formed by thick *light emitting* dies ($>100\mu\text{m}$) and thick substrate. The new method aims at characterizing the interconnects, particularly the solders, without causing any additional damage in the latter. This requirement excludes chemical dissolution of the die or substrate. Indeed, to the best of our knowledge, there is no chemical substance dissolving semiconductor materials without attacking the metallic interconnects.

Thus the scenario depicted in figure 3 was used on samples after reflow soldering (fig. 3a) with one zone of interest shown. A deep hole is excavated in the die by femtosecond laser ablation (fig. 3b). This step leads to the sandwich formed of $20\mu\text{m}$ die-material, the interconnects and the substrate are depicted in figure 3c. This sandwich is submitted to successive FIB milling and image acquisition in planes perpendicular to the y-axis. The following sections detail the different operations.

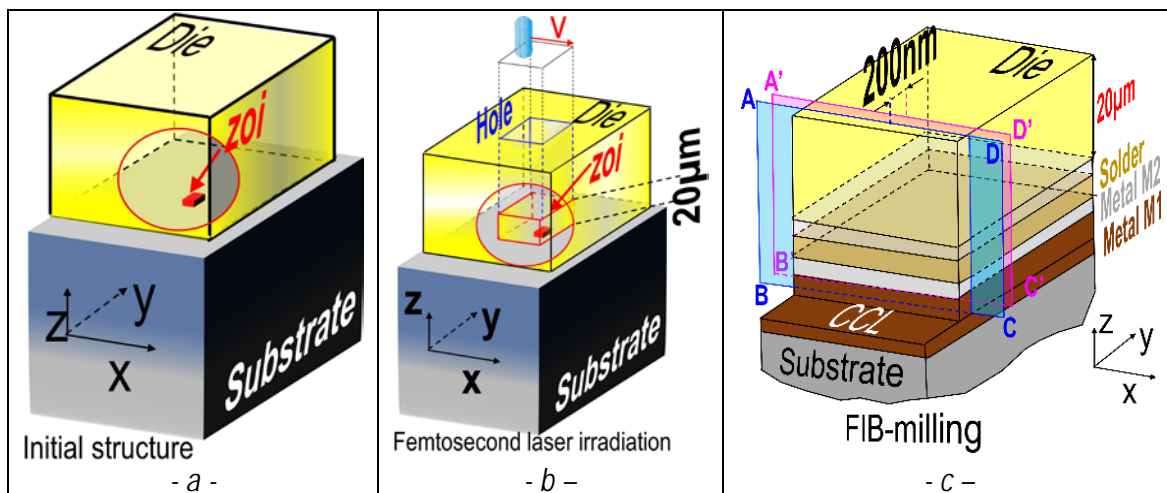
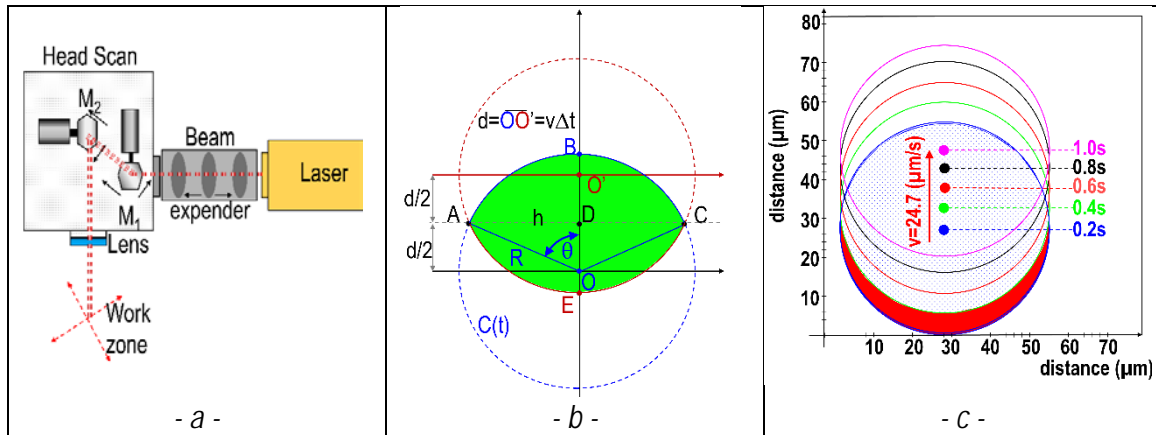


Figure 3: Overall procedure for 3D characterization. (a) The as assembled component after reflow. zoi indicates the zone of interest for further characterization. This is hidden by a thick die-layer. (b) The femtosecond laser produced a deep hole in the die-layer. The zoi is composed of $20\mu\text{m}$ die-material and the underlying interconnects. (c) Zoom in on the volume submitted to FIB milling. SEM observations are done in planes ABCD and A'B'C'D' perpendicular to the y-axis. CCL designates the current circuit layer.

149 3.2.2. Femtosecond laser Die ablation
 150

151 With a 100 W TANGOR (Amplitude Systems) femtosecond laser, rectangular holes with
 152 controlled depths were dug in the die-layer. Figure 4a shows a schematic representation of the test facility.
 153 After passing through an expander with different lenses, the beam (X, Y)-coordinates are controlled
 154 through the displacement of two motorized mirrors (M₁ and M₂). Finally the beam passes through a lens
 155 with a focal distance of 170 mm. A constant spot size is achieved. The beam has a diameter of 55μm at
 156 the intersection with the work zone. Table 3 relates the femtosecond laser characteristics.

157



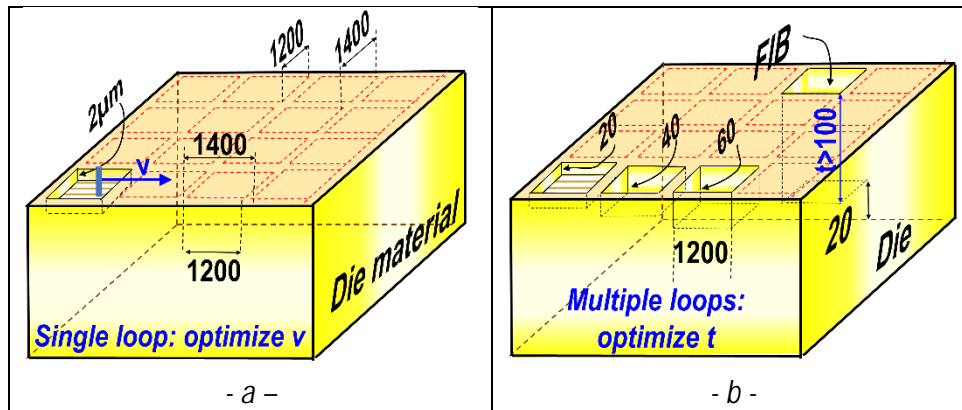
158 **Figure 4:** Hole digging by femtosecond laser ablation. (a) Schematic representation of the test facility.
 159 Laser impact corresponding to the optimized parameters of table 4 (5Hz and 24.7μm/s): (b) two
 160 successive positions of the laser spot in the (x, y)-space. (c) beam displacement along the y-axis is
 161 illustrated during 1s, showing the overlap between successive pulses. The area in red is not ablated; the
 162 dotted area is ablate after 1s.

163
 164 The laser speed v , the pulse duration and frequency as well as the mean power can be
 165 controlled. These parameters were optimized by ablating successive 1200μm wide squares (figure 5) on
 166 the die. Two distinct optimization procedures were used to determine the optimal parameters. First, the
 167 mean power and pulse frequency were set to the values in table 4. Each pulse corresponds to a circle
 168 (55μm diameter) on the work zone. Successive pulses lead to successive circles. The centers of these
 169 circles move with the same speed as the laser (Figure 4b). The laser speed v leading to 2 μm ablation in
 170 a single loop was determined. The pulse frequency and laser speed given in table 4 lead to an overlap
 171 between successive circles (lens ABCE in figure 4b). The area A of the lens ABCD may be expressed as
 172 follows:

173
$$A = 2\arccos\left(\frac{d}{2R}\right)R^2 - d\sqrt{4R^2 - d^2}, d = v\Delta t \quad (1)$$

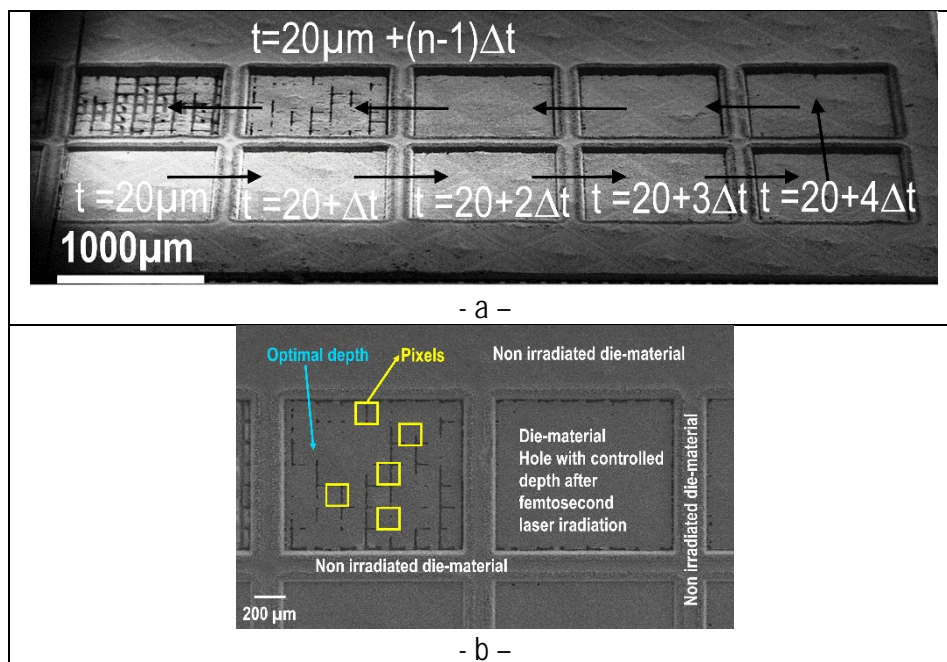
174 R is the spot radius (50μm) and d is the distance between two successive centers of the spot. v and
 175 Δt stand respectively for the laser speed (24.7μm/s) and the time between two laser impacts (0.2s).
 176 This leads to an overlap between two successive impacts of 90.6%. The process parameters being known,
 177 the last optimization step was dedicated to determining the number of loops on each square. We aimed
 178 an ablation depth of 20μm. Successive squares were thus submitted to an increased number of laser
 179 loops (Figure 5b).

180



181 **Figure 5:** Die ablation with femtosecond laser. (a) Determination of the beam velocity to guarantee fixed
 182 ablation thickness for a single loop. (b) Determination of the maximum ablation depth ensuring
 183 undamaged interconnects.

184 Figure 6a shows a SEM observation with squares of successively deeper grooves in the die.
 185 The process was stopped in the square corresponding to the desired ablation depth. Figure 6b shows
 186 SEM observations of the last ablated squares. The ablation depths as well as the remaining die-material
 187 layer were checked thoroughly on the die. Once all the ablation parameters were determined, the
 188 procedure was repeated in the center of the die with the desired ablation depth, leaving 20μm thickness.
 189 This left the component ready for FIB milling.
 190



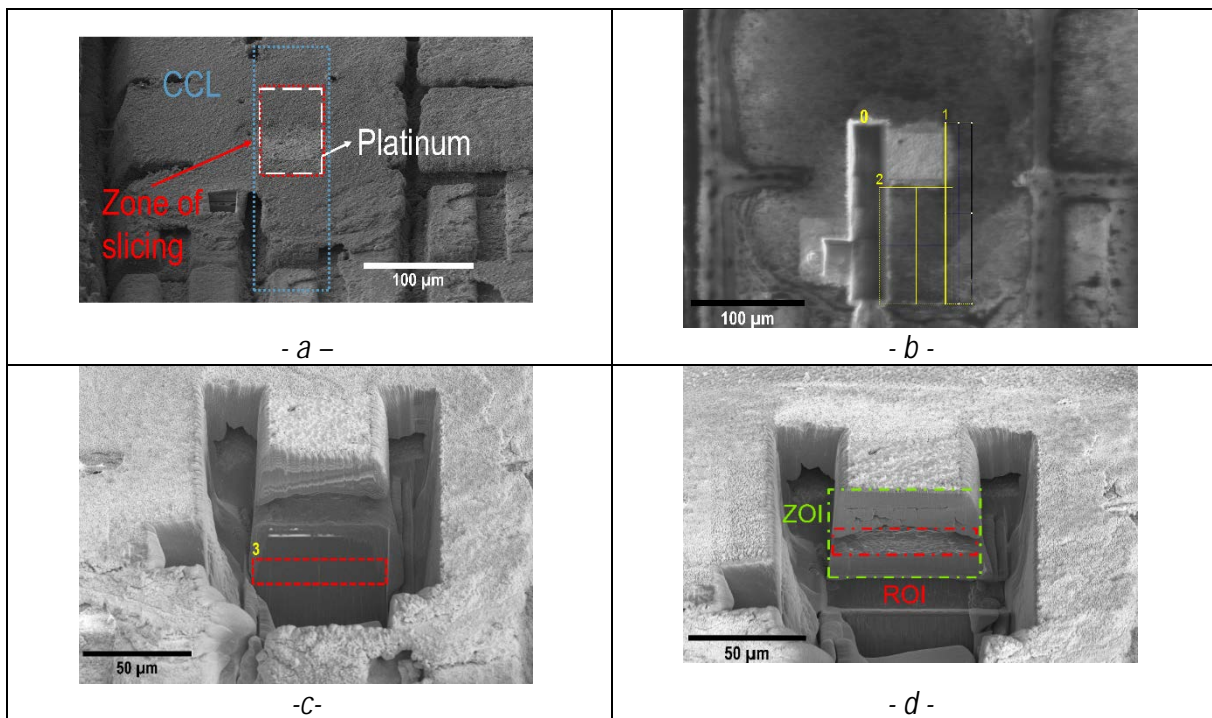
191 **Figure 6:** (a) Optimization of laser ablation procedure. SEM observations on the die used for
 192 determining the optimized parameters. Successively increased ablation depths ($t = 20\mu\text{m} + \Delta t$) in
 193 each square, (b) and (c) zoom in on the last squares ablated.

195 3.2.3. FIB milling and image acquisition

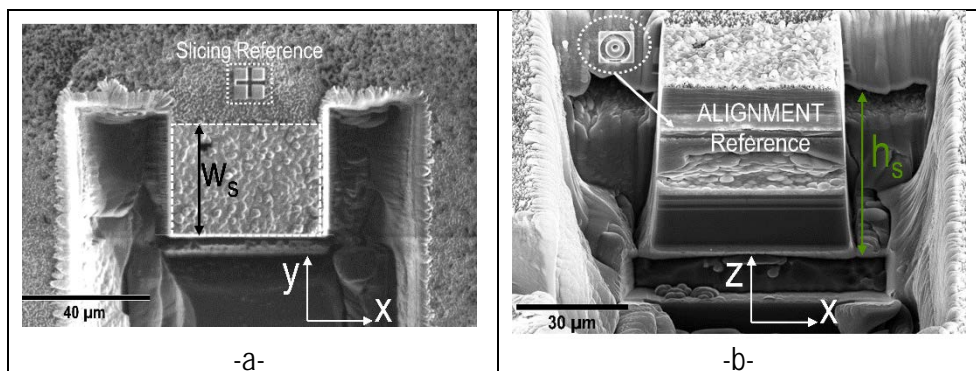
196 The optimal ablation parameters were applied at the center of the die (fig. 7a). The analysis was
 197 done on the solder marked by a blue dashed line. A red dashed line illustrates the zone of slicing
 198 corresponding to the whole solder.
 199

200 First platinum is deposited (white dashed line) gradually along the solder length in order to
 201 reduce curtaining effects during the slicing. During platinum deposition, the current is fixed at 0.77nA and
 202 the voltage at 30kV. Then material milling is operated in zones 0-2 under 65nA (figures 7b, c). Figure 7b
 203 shows an intermediate state. The milling in zone 0 is completed. The milling of zone 2 is in progress and
 204 the milling of zone 1 has to be done. Milling of zone 3 (fig. 7c) was added to decrease the slicing time
 205 later on. Before beginning the second step, the ZOI (Zone of Interest) is cleaned by slicing four times with
 206 21 nA. Table 6 gives all the detailed values of current, voltage and time interval for each sub-step.

207 In the last step prior to slicing (Figure 8), the slicing width (w_s), height (h_s) and direction are
 208 defined. Each image contains a fiducial as shown in figure 8. Figure 8a depicts the fiducial (cross) used
 209 as slicing reference. The image with this cross and the zone of slicing (white dashed line) is used by the
 210 slicing software as reference for the (xy) plane. The size of the slices in the (x, y) plane, the milling time
 211 (related to the milling depth in the y direction) and the relative position of the milling area and the fiducial
 212 are defined at this instant. The slices are 200 nm thick in the y direction. The other fiducial (figure 8b) as
 213 well as the zone of interest (zoi) are defined on a second image. During image acquisition, the same tilt
 214 angle as during subsequent slicing is used. The two fiducials are constructed by platinum deposition (table
 215 7). At this stage, the width (w_s) and height of slicing (h_s) are defined. The milling depth for each step has
 216 been defined previously.



217 **Figure 7: (a) Slicing zone localization, (b) Digging around one pad, (c)-(d) definition of ZOI and ROI**
 218

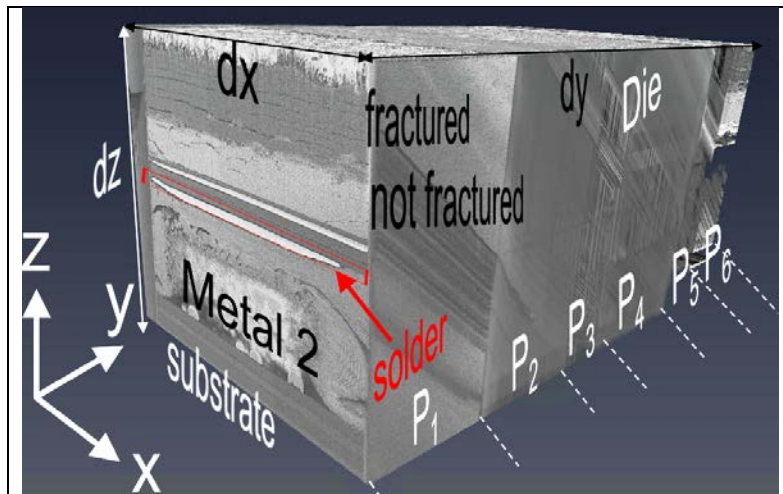


219 **Figure 8:** Definition of fiducials (a) with the zone of slicing in the (x, y)-plane, (b) with the zone of interest
220 in the (x,z)-plane.
221

222 After deposition of the fiducials, more than 400 slices (2.5nA, 30kV) were milled and image
223 acquisition done for each slice. Each milling operation took 30s per slice. In addition, for each slice the
224 acquisition time was about 1 min.

225
226 **4. Results:**
227 **4.1 3D solder observation after reflow**
228

229 The complete solder volume has been analyzed with a voxel size controlled by the SEM
230 resolution in the (x, z) plane and of $l_y=200\text{nm}$ in the y (slicing) direction. Image acquisition was done with
231 a tilt angle of 52° , leading to a slightly larger voxel size in the z than in the x-direction ($l_x=18\text{nm}$, $l_z=23\text{nm}$).
232 Each slice, in the (x, z)-plane, the image dimensions contains more than 2500 pixels in the x-direction
233 and more than 1500 pixels in the z direction, corresponding (with the tilt correction) to $d_x=55.3\mu\text{m}$ and
234 $d_z=47.1\mu\text{m}$ (figure 9). 530 slices were analyzed with Amira and a 3D reconstruction was achieved. Figure
235 9 shows the total volume observed. The total volume reconstructed in the y direction corresponds to
236 $90\mu\text{m}$.



237 **Figure 9:** 3D reconstruction of the total observed volume ($d_x=55.3\mu\text{m}$, $d_y=90\mu\text{m}$, $d_z=47.1\mu\text{m}$). The
238 solder is indicated by the red rectangle.
239

240 About $20\mu\text{m}$ die-material was left above the interconnects. Equidistant cracks are observed in
241 the upper part of the die (Figure 9). This corresponds to the successive loops of the laser impacts with
242 layer thickness of about $2\mu\text{m}$. However, the die-material close to the interconnects is not damaged (Figure
243 9). After cracking, the fractured layers of die-material act as a buffer (damper) and protect the underlying
244 material from damage. Henceforth, we assume no significant damage is induced in the solder material by
245 the laser impacts. However, today, to our knowledge no mechanical model of the effects of laser impacts
246 on complex structures exists. With this technique, the total solder height is observed at high magnification
247 (pixel size: $l_x=18\text{nm}$, $l_z=23\text{nm}$).

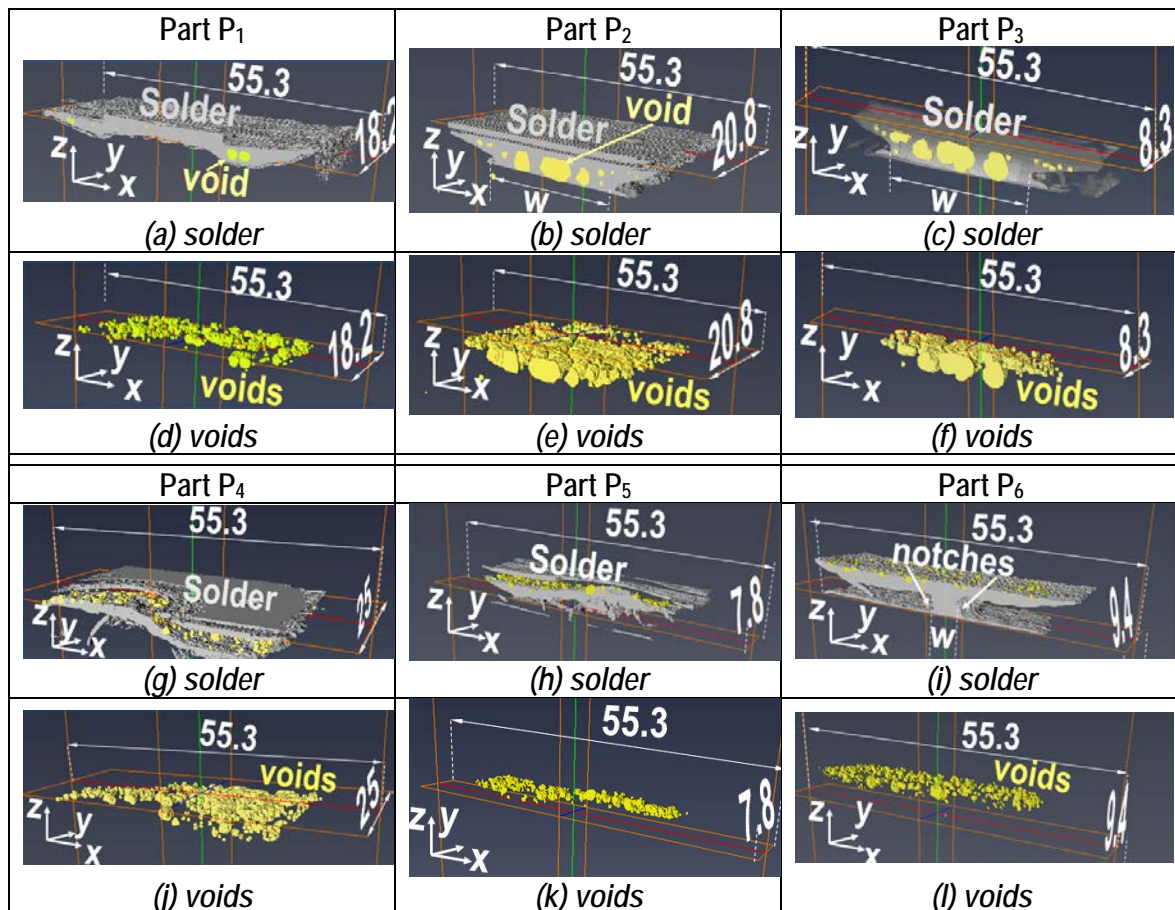
248 In the following, 3D reconstructions of the solder are analyzed. Due to its small height compared
249 to the two other dimensions, we decided to consider six connected parts (P_1 to P_6). The best 3D
250 representation we could make out dictated the width (in the y direction) of each individual part. Figure 10
251 depicts 3D reconstructions of the solder material and the voids present in each part. All the dimensions
252 are given in μm . $55.3\mu\text{m}$ corresponds to the milling width in the x direction. The solder fits in this
253 observation window. The total width in the y direction of all the parts sums up to $90\mu\text{m}$. Moving from part
254 P_1 to part P_6 , reveals a significant variation in the outer shape of the solder volume. In part P_1 , no notch

255 is visible. Parts P_2 to P_6 develop notches on both sides of the solder. The width w of minimum material
 256 layer decreases significantly from part P_1 to P_6 . Part P_6 exhibits extremely deep notches. These extremely
 257 strong variations in the solder geometry can only be observed by a 3D SEM-based high-resolution
 258 tomography.

259 High-resolution tomography not only allows reconstruction of the 3D volume, but also to analyze
 260 independently all the 530 slices separated by 200nm in the y direction. Some examples highlighting the
 261 powerfulness of tomography with an SEM-resolution are given below.

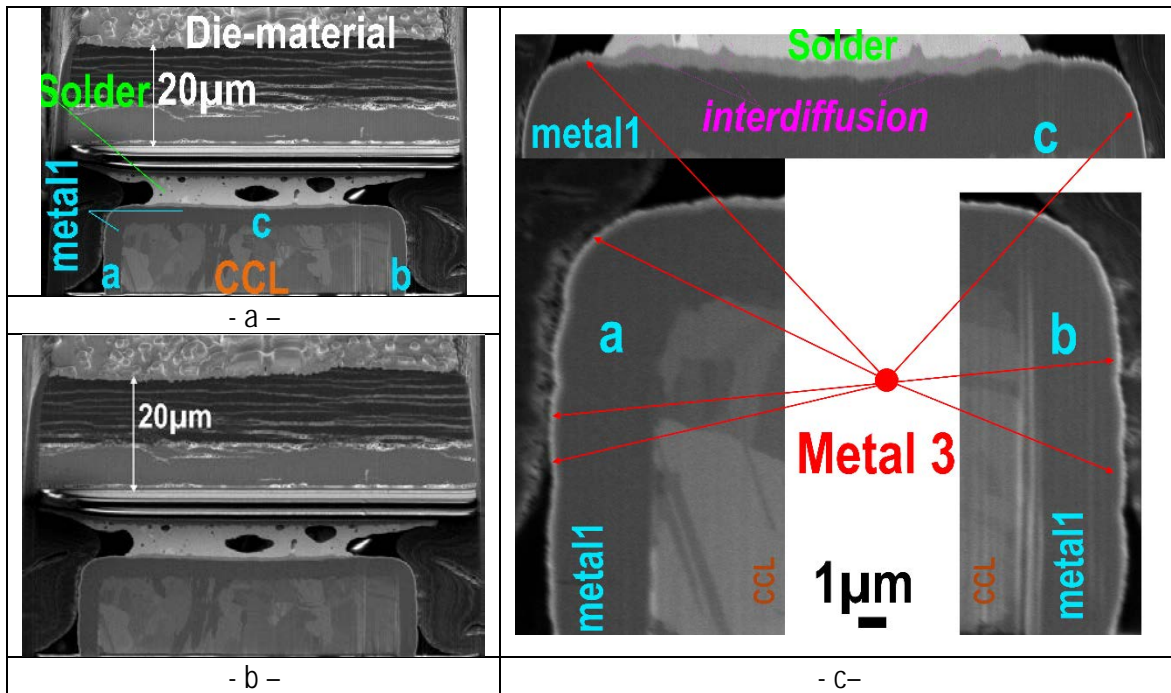
262 Figure 11 depicts one of the 530 sections. Figure 11a shows the entire section. Before focusing on
 263 the ROI (region of interest), centered on the solder material, we consider the different material layers.
 264 EDX analyses were done in this and similar sections. On figure 11a, the locations of the CCL, the wetting
 265 material 1 and wetting material 3 are indicated. Figure 11b offers a zoom of regions a, b and c. Clearly,
 266 metal 3 covers all the outer CCL borders. All over the entire joint between the CCL and solder, metal 3 is
 267 present and nice interdiffusion operated. Note that only the high SEM resolution allows checking the
 268 presence of the submicron sized metal 3-layer. At this stage, one could assume a perfect solder CCL-
 269 interface. The situation will change dramatically in the next paragraph.

270



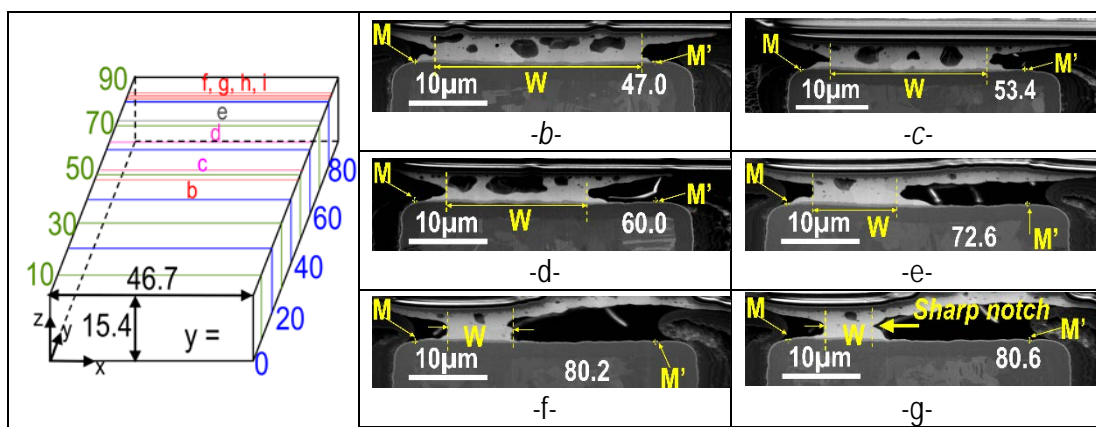
271 **Figure 10:** 3D reconstruction of the total solder volume ($dx=55.3\mu\text{m}$, $dy=90\mu\text{m}$, $dz=47.1\mu\text{m}$). Each part
 272 (P_1 to P_6) is depicted separately. For all the parts, two images are shown. The first shows the solder
 273 volume. The second depicts the voids inside the solder. All dimensions are given in μm .

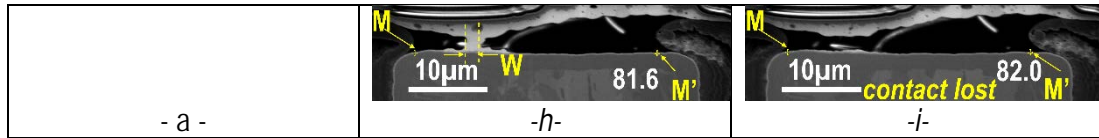
274
 275
 276
 277
 278
 279



280 *Figure 11: SEM-observation of one typical slice. (a) The total observed section (ZOI) with the main*
 281 *materials detectable in this section. (b) The same section without annotations (c) Zoom in on the*
 282 *boundaries to highlight the perfect covering by metal 3 of the entire CCL boundary.*
 283

284 Figure 11 highlighted the paramount importance of SEM resolution on a single cross section. The
 285 same analysis was done on all the 530 cross sections. Figure 12 depicts specific sections particularly
 286 useful for qualifying the reflow process. Figure 12a depicts a sketch of the entire ROI with the location of
 287 slices b to i. First, the maximum width w of the solder at the CCL interface was determined considering
 288 all the slices. Points M and M' indicate the largest segment observed at the solder CCL-interface (Figure
 289 12b). The interface covered with solder material decreases between slices b and h. Finally, at section i
 290 starts a no contact area. As mentioned in the previous paragraph, the distribution of wetting metal all over
 291 the CCL reveals satisfying. Thus, wetting does not explain the strong evolution of the contact between
 292 CCL and solder. Instead, we reveal a local disorientation between the upper part (die) and lower part
 293 CCL. Slices e to i reveal large distances between the upper CCL border and lower solder border. Present
 294 sections show much larger gaps to be covered by the solder material. Relative rotation between the CCL
 295 and upper part of the component (die) may be the cause of these distances. Imperfect soldering leads to
 296 deep notches. Figure 12g shows a very sharp notch.
 297





298 **Figure 12:** SEM-observations after soldering. (a) Schematic representation of the solder indicating the
 299 location of the different sections. (b-i) Cross sectional observations of the solder.

300

301

302

303

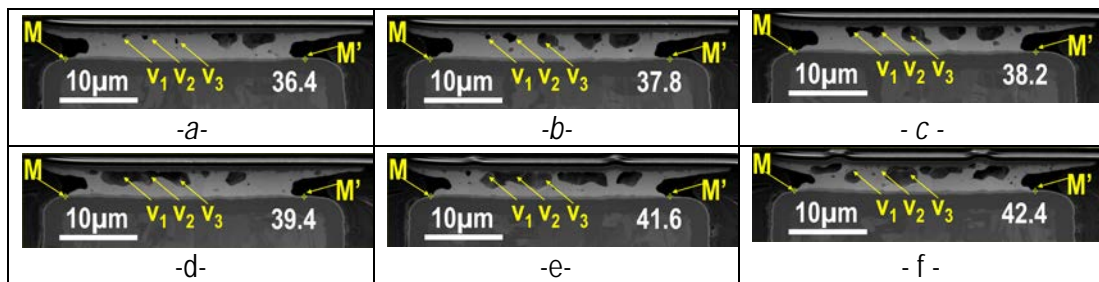
304

305

306

307

The last example shows the advantage of high resolution in the slicing direction (0.2µm). Figure 13 depicts SEM observations on slices very close to each other. One single observation (Figure 13a) would lead to consider three independent voids marked v_1 to v_3 . On the following slices, these micro-voids coalesce geometrically to form a single one. In addition, on the last slice shown they appear as independent voids. Analyzing void interaction is of primary importance when dealing with solders containing large via holes. The latter combine with micro-voids caused by the soldering process.



308 **Figure 13:** SEM-observations after soldering. Geometric coalescence of micro-voids. (a-b) 3
 309 independent voids v_1 , v_2 , v_3 are observed. (c) v_1 and v_2 coalesced. (d-e) v_1 , v_2 , v_3 form a single void. (f)
 310 v_1 , v_2 , v_3 appear disconnected.

311

5. Discussion

312

313

314

315

316

317

318

319

320

321

322

323

324

325

326

327

328

329

330

331

332

333

334

335

The purpose of present work was the development of a novel inspection method allowing characterizing solders embedded in a complex architecture without disassembling the component. The first step consists of digging a hole of controlled dimension by femtosecond laser irradiation. This procedure was optimized in order to minimize the remaining layer of die-material while ensuring a small height of the latter was not fractured. The second step consists of successive FIB milling (slicing) and image acquisition. The last step consists of 3D reconstruction of the slices.

The optimized process parameters are given in table 4. After laser ablation, the interconnects are still covered by a 20µm thick layer of die material. The outermost 10µm of die-material exhibit a layered structure with an approximate thickness of 2µm. The last 10µm do not reveal damage in all the observed 530 slices. We assume thus that the material beneath is not affected by the successive laser impacts. A theoretical analysis of successive laser impacts and consequent material ablation might be considered in future work.

After determining the optimized parameters for the femtosecond laser ablation, the total FIB milling and image acquisition required a week. Smaller distances between successive slices would of course increase this time. However, the milling time does not increase linearly with the number of slices. A large part of the FIB milling time corresponds to the sample preparation detailed in figure 8.

The analysis of only one solder is presented in present paper. The results allow however to draw significant conclusions on the reflow assembling process. The high-resolution SEM images confirm the presence of a wetting metal layer all around the CCL in all the 530 slices. This submicron layer is of course only detectable by SEM or TEM observations. Present analysis revealed however severe damage in the solder. The successive slices in figure 12 show a strong variation in the distance between the CCL and the upper part of the component. This indicates clearly a misalignment between the lower and upper part of the LED during reflow assembling. This effect can, of course, not be simulated on single solders or on

336 smaller architectures. Present method allowing damage characterization on the final product architecture
337 is thus useful when developing new designs.

338 The new inspection method was applied to a particular solder in a particular opto-electronic
339 component in order to show the feasibility and in order to highlight the need of 3D characterization of the
340 solders. The data given in tables 1 to 3 are specific to the microscope and laser used. The reader can
341 find the optimized parameters in tables 4 to 7. The same method may be easily adapted to other opto-
342 electronic components. Only a few parameters have to be adapted to the particular substrate material.
343 The determination of the specific overlap of the laser beam (table 4) may be determined on the substrate
344 material without the presence of the opto-electronic component.

345 The purpose of present analysis is a very close description of the damage consequent to the
346 assembling process. Observing a single solder revealed the large variation in geometry of the latter. The
347 test is thought to be an advanced control for soldering complex architectures. Nevertheless, the results
348 give indications on potential mechanical models of the component. The huge variations in solder geometry
349 hint to a statistical approach. In a solder complex shaped notches, via holes and micro-voids interact.
350 With new FIB technology allowing faster milling, a large number of observations (slices) might be the first
351 step to a database for artificial intelligence algorithms of the soldering process.

352

353 6. Conclusions

354

355 Assembling products with numerous interconnects by reflow is challenging. Solder materials
356 have been largely studied in the last decade. The present work addressed the issue of characterizing any
357 chosen solder in the as assembled condition of a complex architecture. An experimental LED was
358 dissected by femtosecond laser irradiating the die-material layer. After optimizing the femtosecond laser
359 parameters, a deep hole was obtained in the die-material layer. Then, successive FIB milling on 200nm
360 distant slices and image acquisition on a scanning electron microscope were made. 530 SEM
361 observations of a single solder were obtained. Amira allowed 3D reconstruction.

362 All the SEM observations show that no damage in the solders was induced by the preparation
363 techniques. The high-resolution 3D tomography combined with EDX observations allows otherwise
364 impossible characterizations of submicron material layers. As an illustration, the presence of wetting metal
365 surrounding the current circuit layer (CCL) was confirmed in present work. The small distance between
366 successive slices (200nm) is particularly well adapted for characterizing the heterogeneities of different
367 submicron material layers or heterogeneities of solder geometry in microelectronics. As an example,
368 present work revealed micro-void coalescence in the solder material. This ability of the new tool is of
369 primary importance to analyze the influence of solder design (e.g. the presence of via holes).

370 Finally, the primary importance of characterizing the solders in the real assembled architecture
371 was shown. Covering the total solder length with high-resolution slices allowed detecting an abnormal
372 distance between the lower and upper part of the component. Thus, present work identified clearly, which
373 problems occurred during the reflow soldering process. The same technique can be applied fruitfully after
374 special test loadings during product development (thermal cycles or thermal shock cycle loading) of the
375 component. If the time needed for the characterization might seem large at first glance, dividing the total
376 time by the number of slices (SEM images) shows the efficiency of the present method.

377

378

379

379 References

380

- 381 [1] Coushaine et al. United States US 20050281 033A1 (12) Patent Application Publication (10) Pub.
382 No.: US 2005/0281033 A1Coushaine et al. (43) Pub. Date: Dec. 22, 2005
383 [2] Glazer J. Microstructure and mechanical properties of Pb-free solder alloys for low-cost electronic
384 assembly: a review. J Electron Mater. 1994; 23:693–700.

- 385 [3] Abteu M, Selvaduray G. Lead-free solders in microelectronics. *Mater Sci Eng R*. 2000; 27:95–
386 141.
- 387 [4] Grossmann G, Tharian J, Jud P, Sennhauser U. Microstructural investigation of lead-free BGAs
388 soldered with tin-lead solder. *Solder Surf Mt Technol*. 2005; 17:10–21.
- 389 [5] Zhang Q., Investigations on Microstructure and Mechanical Properties of the Cu/Pb-free Solder
390 Joint Interfaces, Doctoral Thesis accepted by University of Chinese Academy of Sciences,
391 Beijing, China, ISSN 2190-5053, Springer Theses, ISBN 978-3-662-48821-8, DOI 10.1007/978-3-
392 662-48823-2.
- 393 [6] Laurila T, Vuorinen V, Kivilahti JK. Interfacial reactions between lead-free solders and common
394 base materials. *Mater Sci Eng R*. 2005;49:1–60.
- 395 [7] Laurila T, Vuorinen V, Paulasto-Kröckel M. Impurity and alloying effects on interfacial reaction
396 layers in Pb-free soldering. *Mater Sci Eng R*. 2010;68:1–38.
- 397 [8] Gao F, Nishikawa H, Takemoto T. Intermetallics evolution in Sn–3.5Ag based lead-free solder
398 matrix on an OSPCu finish. *J Electron Mater*. 2007;36:1630–4
- 399 [9] Ventura T, Terzi S, Rappaz M, Dahle AK. Effects of solidification kinetics on microstructure
400 formation in binary Sn–Cu solder alloys. *Acta Mater*. 2011;59:1651–8.
- 401 [10] Roshanghias A., Vrestal J., Yakymovych A., Richter K.W., Ipser H. (2015), Sn–Ag–Cu
402 nanosolders: Melting behavior and phase diagram prediction in the Sn-rich corner of the ternary
403 system, in CALPHAD: Computer Coupling of Phase Diagrams and Thermochemistry, 49: 101-
404 109
- 405 [11] Lee T.K., Bieler T.R. (2015), Fundamentals of Lead-Free Solder Interconnect, From
406 Microstructures to Reliability, Springer New York Heidelberg Dordrecht London, ISBN 978-1-
407 4614-9265-8, DOI 10.1007/978-1-4614-9266-5.
- 408 [12] Lee T.K., Bieler T.R. (2017), Lead free solder Reference Module in Materials Science and
409 Materials Engineering, doi:10.1016/B978-0-12-803581-8.09205-5, 1-12.
- 410 [13] Mei Z, Morris JW Jr. Characterization of eutectic Sn–Bi solder joints. *J Electron Mater*. 1992;
411 21:599–607.
- 412 [14] McCormack M, Jin S, Kammlott GW, Chen HS. New Pb-free solder alloy with superior
413 mechanical properties. *Appl Phys Lett*. 1993;63:15–7.
- 414 [15] Liu PL, Shang JK. Interfacial embrittlement by bismuth segregation in copper/tin–bismuth Pb-free
415 solder interconnect. *J Mater Res*. 2001;16:1651–9.
- 416 [16] Zeng K, Tu KN. Six cases of reliability study of Pb-free solder joints in electronic packaging
417 technology. *Mater Sci Eng R*. 2002;38:55–105.
- 418 [17] Suo Z., Reliability of Interconnect Structures, pp. 265-324 in Volume 8: Interfacial and Nanoscale
419 Failure (W. Gerberich, W. Yang, Editors), Comprehensive Structural Integrity (I. Milne, R.O.
420 Ritchie, B. Karihaloo, Editors-in-Chief), Elsevier, Amsterdam, 2003.
- 421 [18] Chan YC, Yang D. Failure mechanisms of solder interconnects under current stressing in
422 advanced electronic packages. *Prog Mater Sci*. 2010;55:428–75.

- 423 [19] Kloppenburg G., Wolf A., Lachmayer R., (2016), High-resolution vehicle headlamps: technologies
424 and scanning prototype, *Adv. Opt. Techn.* 2016; 5(2): 147–155.
- 425 [20] Braess H.-H., Seiffert U., (2013), *Vieweg-Handbuch Kraftfahrzeugtechnik*, ISBN 978-3-658-
426 01690-6 Springer Vieweg, Wiesbaden, (2013),chapter 8: 902-905.
- 427 [21] Berlitz S., Hamm M., Funk C., *Matrix-LED-Scheinwerfer von Audi*, *Automobiltechnische*
428 *Zeitschrift*, 116, 10–15 (2014).
- 429 [22] Habib S., Hannan M.A., Javadi M.S., Samad S.A., Muad AM., Hussain A. (2013), *Inter -Vehicle*
430 *Wireless Communications Technologies, Issues and Challenges*, *Information Technology Journal*
431 12 (4): 558-568.
- 432 [23] Liu C., Sadeghi B., Knightly E.W., (2011), *Enabling Vehicular Visible Light Communication*
433 *(V2LC) Networks*, *Proc. ACM Int'l. Wksp. Vehic. Inter-Networking*, pp. 41–50.
- 434 [24] Yu S.-H., Shih O., Tsai H.-M. , *Smart Automotive Lighting for Vehicle Safety*, *VISIBLE LIGHT*
435 *COMMUNICATIONS: THE ROAD TO STANDARDIZATION AND COMMERCIALIZATION*, *IEEE*
436 *Communications Magazine*, December 2013, p. 50-59.
- 437 [25] Meijerl J., Du K., Gillner A., Hoffmann D., Kovalenko V.S., Masuzawa T., Ostendorf A., Poprawe
438 R., Schulz W., *Laser Machining by short and ultrashort pulses, state of the art and new*
439 *opportunities in the age of the photons*, *CIRP Annals*, Volume 51, Issue 2, 2002, Pages 531-550.
- 440 [26] Stevie F. A., Shane T. C., Kahora P. M., Hull R., Bahn D., Kannan C. and David E., *Applications*
441 *of Focused Ion Beams in Microelectronics Production, Design and Development*, *Surface and*
442 *interface analysis*, VOL. 23, 61-68 (1995).
- 443 [27] S. Nocairi, K. Maarouf, Ch. Roucoules, G. Kermouche, S. Sao-Joao, H. Klöcker, *Automotive*
444 *optoelectronic components submitted to thermal shock: Impact of component architecture on*
445 *mechanical reliability*, *Microelectronics Reliability* 128 (2022) 114422
446 <https://doi.org/10.1016/j.microrel.2021.114422>.
- 447 [28] A. Tireira, G. Requena, S. Sao Jao, A. Borbely , H. Klöcker, *Rupture of intermetallic networks and*
448 *strain localization in cast AISi12Ni alloy: 2D and 3D characterization*, *Acta Materialia* 112 (2016)
449 162-170.
- 450 [29] A. Tireira, M. Bornert, G. Requena, E. Maire, S. Sao Jao, A. Borbely , H. Klöcker, *Damage in a cast*
451 *AISi12Ni alloy: In situ tomography, 2D and 3D image correlation*,
452 <https://doi.org/10.1016/j.mtla.2019.100475>.
- 453 [30] A. Fraczekiewicz, F. Lorut, G. Audoit, E. Boller, E. Capria, P. Cloetens, J. Da Silva, A. Farcy, T.
454 Mourier, F. Ponthenier, P. Bleuet, *3D high resolution imaging for microelectronics: a multi-*
455 *technique survey on copper pillars*, *Ultramicroscopy* (2018), doi: 10.1016/j.ultramicro.2018.04.012
456

457
458

Tables

Inputs	WD (mm)	Tilt (θ°)	Signal	EHT(kV)
Values	17~20	58~62	AsB/SE2	20

459
460

Table 1: Zeiss SEM configuration parameters

Parameters	Modes	Ar Gas valve	Voltage (kV)	Time (Hours)
Values	Normal (Basic)	6.9-7.7	6	4-11
	Fine	8-8.8	4	1-2

461
462

Table 2: Cross polisher parameters

Source Type	Laser Wavelength	Pulse Duration	Laser Frequency
TANGOR 100 W	1030 nm	500~600 fs	5kHz

463
464

Table 3: Femto second laser characteristics

Frequency (Hz)	\varnothing spot (μm)	Mean Power (W)	Overlap (%)	Speed ($\mu\text{m/s}$)
5	55	0.16	>70%(optimized)	24.7

465
466

Table 4: Die-ablating procedure: parameters

FIB Type	Ion	Voltage (kV)	FEG SEM of FIB		
Thermo Scientific Helios Nano Lab 600i Dual Beam	Gallium	30	Detectors	Voltage(kV)	WD (mm)
			Secondary electron	<10 (optimized)	4.2

467
468

Table 5: Focused Ion Beam technical parameters

	Pt deposition	Material milling around ZOI	Cleaning before slicing
Current (nA)	0.77	65	21
Voltage (kV)	30	30	30
Duration	40~50 (mins)	1 day	1~3 (mins)

469
470
471

Table 6: Material-milling parameters for ZOI preparation

	Pt-thickness (μm)	Current (nA)	
		Pt deposition	imprint digging
Slicing reference	2	0.4	2.5
Alignment reference	1	0.4	2.5

472
473

Table 7: Fiducials parameters